DOI: ADD DOINUMBER HERE

Dynamic Simulation and Control Design of Hybrid Electric Powertrain Architectures

Silvan Keim*
*Institute of System Architectures in Aeronautics, German Aerospace Center (DLR)
Weβling, Germany
silvan.keim@dlr.de

Abstract

This paper presents component modeling and dynamic simulation of a hybrid electric powertrain architectures for future electric aircraft, containing fuel cells, batteries, electric motors and power electronics. The focus of the component modeling using Modelica is the individual dynamic behaviour in order to get a representative dynamic behavior of the whole system. This enables the implementation and test of different power distribution control methods as well as component sizing. The resulting good understanding of the system behavior leads to an early detection of potential design problems and can contribute to the development of a better system design

1. Introduction

In order to reduce climate impact in aviation, developments of hybrid or fully electric propulsion systems are required. Hybrid electric propulsion systems offer a wide variety of possible architectures and operation strategies. To get a better understanding of the system behaviour and to be able to compare different configurations, a powertrain model has been developed in Modelica. Modelica is a function based programming language to model physical systems e.g. fluid systems, mechanical systems or electrical systems. The considered architectures are based on fuel cells (FC) as the main power source and batteries or supercapacitors as the secondary power source. As the maximum current slope of the FC is limited due to fuel starvation, the dynamic behavior of fuel cells is much slower compared to gas turbines or batteries.¹⁷ Therefore, the electric system must have at least one secondary power source to achieve a fast dynamic response when the required power of the electric motors suddenly increases e.g. at take-off or go-around.¹⁷ There are various factors influencing the power distribution control design in terms of lifetime and efficiency. The FC has very low efficiency at low and high power loads and has its highest efficiency at medium power load.¹⁰ The FC lifetime is mainly decreased at high load, light load and high load variation rate.¹⁰ The battery lifetime is influenced by the depth of discharge and occurring maximum C-rates.¹⁰ Voltage conversion ratio as well as load and minimum input voltage of the DC-DC converters also have an impact on their efficiency and other components.⁵

The main purpose of the powertrain model is to evaluate, compare and optimise the performance of different powertrain architectures in terms of overall efficiency and mass in steady-state and transient conditions. In case of simple systems, analytical optimisations may be sufficient, but with an increasing system complexity, the risk of missing important constraints and dependencies resulting in wrong results is increasing rapidly. A dynamic simulation with models containing all important parameters and dependencies significantly reduces the risk of errors and increases the flexibility. It offers the possibility to easily check important constraints and to change system typologies while maintaining all dependencies and can even detect critical operation points or behaviours by simulating gate to gate missions.

Several studies have addressed hybrid electric powertrain simulations with different configurations and controls using different modeling fidelity. Li et al¹⁰ compares four different topologies of aircraft power systems in terms of hydrogen consumption, FC efficiency and FC and battery aging. The behavior of the power sources in a hybrid electric propulsion system for a UAV was simulated in Lee et al⁹. The propulsion system of the target UAV consists of solar cells, fuel cells, and a battery. In addition, the simulation was verified with the flight test data, which has a hybrid propulsion system consisting of a fuel cell and battery. Different control concepts are tested by simulating a fuel cell vehicle with a battery or a supercapacitor storage device by Thounthong et al¹⁷. A model of a three source hybrid electric propulsion system with similar architectures also containing battery, FC and gas turbine are presented by Grazioso et al⁶. A turboprop hybrid electric propulsion system is modeled and investigated by Cameretti et al² also including battery sizing. A survey on aircraft hybrid electric propulsion presenting the state-of-the-art technologies

and future tendencies including different topologies, energy storages and control strategies are presented by Rendon et al¹⁵.

2. Component Modeling

In order to understand the behavior of the powertrain model, the following section explains the parameters and equations included in the individual components. Use cases of the powertrain simulation are tests of different control concepts, calculation of overall mission efficiencies and verification of component sizing. While stationary components would be sufficient for efficiency calculations, dynamic behaviour is important for control tests and component sizing. Therefore, the focus of the component modeling lies on the particular component dynamics.

2.1 Battery

The Battery model is a thevenin second order model with an equivalent electric circuit explained e. g. in Xia et al²¹, containing the state of charge (SOC) dependent open circuit voltage, an internal resistance and two RC elements, responsible for the dynamic response of the battery. Different parameter sets can be stored, representing different battery types like Nickel Cobalt Aluminum (NCA), Nickel Manganese Cobalt (NMC) or Lithium Titanate (LTO). Especially the LTO chemistry, allowing maximum discharge rates of up to 20 C³, might be interesting in terms of weight, when the battery is only used as an auxiliary battery with a high power density demand as described in Section 4. There are several papers measuring cell behaviours and fitting parameters to the components of the equivalent electric circuit with different results. Relative consistent and extensive measurements even varying the C-rate between $0.25\,\mathrm{C}$ and $4\,\mathrm{C}$ are described in Madani et al 12 . As the battery model is used at high discharge rates, the parameterset with the highest measured discharge rate of 4C is used. Measurements at different C-rates provide the possibility to implement a C-rate dependency of parameters, but in this case with high uncertainty as the parameters would have to be extrapolated up to 20 C. As a comparison to more conventional Li-ion batteries like NMC, LMO, NCA etc. the results of the measurements of an NMC battery cell of Tran et al²⁰ is used. The resulting dynamic behavior of the two battery types are shown in figure 1 by observing the cell voltage response during a charge and discharge with defined current pulses. They are both charged and discharged with their maximum allowed C-rate which is 1C for the NMC battery and 20C for the LTO battery, leading to different time scales. The dynamic behavior is quite different. The influence of the individual electric circuit components can be observed on the pack voltage response: the open circuit voltage, the additional voltage steps during charge and discharge because of the internal resistance and time dependent effects as a result of the capacitances.

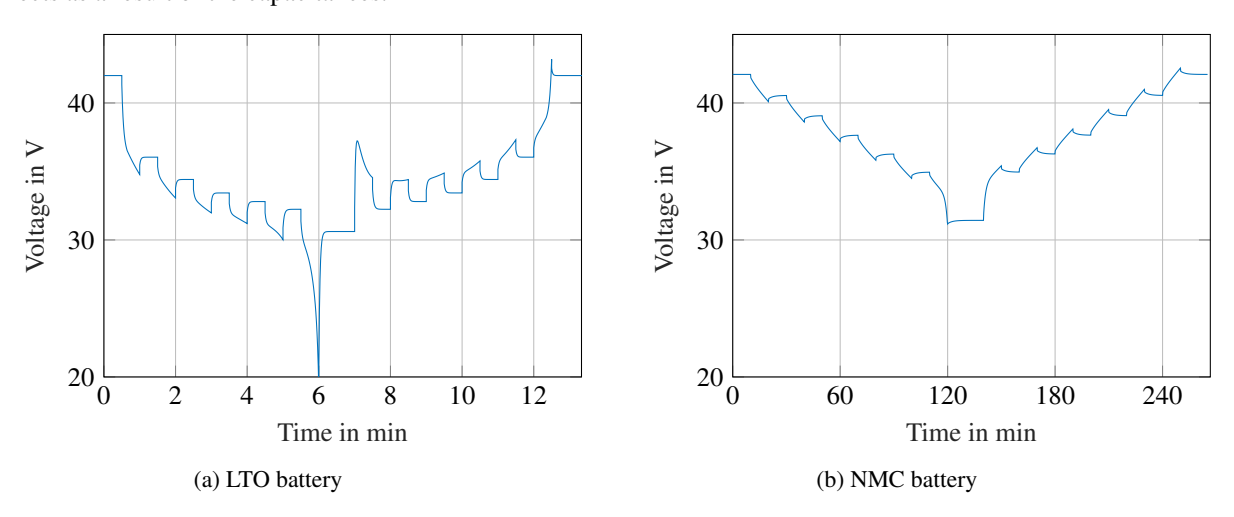


Figure 1: Dynamic voltage response of the LTO battery model in (a) and the NMC battery model in (b).

2.2 Fuel Cell

The proton exchange membrane (PEM) FC model output on the electric side is a current dependent voltage, based on the polarization curve and affected by the FC area and number of serial cells. The polarization curve is calculated using the open circuit voltage (OCV) and several loss mechanisms. The OCV is calculated using eq. (1) (Nernst equation) with a standard cell potential E_0 of $1.219V^{13}$, corrected by the influence of temperature and pressure:

$$U_{\text{OCV}} = E_0 - e_T (T - T_0) - \frac{RT}{2F} \ln \left(\frac{p_{\text{H}_2\text{O}}}{p_{\text{H}_2} p_{\text{O}_2}^{1/2}} \right)$$
 (1)

where E_0 is the standard cell potential, e_T is the temperature coefficient, T is the operating temperature, T_0 is the standard temperature, T_0 is the universal gas constant, T_0 is Faraday's constant and T_0 , T_0 and T_0 are the normalized partial pressures of water, hydrogen and oxygen. The use of air instead of pure oxygen reduces the reversible voltage by T_0 and T_0 is then corrected by current density dependent activation losses, ohmic losses and concentration losses according to eq. (2) resulting in the typical polarization curve:

$$U_{\text{cell}} = U_{\text{OCV}} - \eta_{\text{act}} - \eta_{\text{ohm}} - \eta_{\text{con}}$$
 (2)

where U_{cell} is the cell voltage, U_{OCV} is the open circuit voltage, η_{act} are the activation losses, η_{ohm} are the omic losses and η_{con} are the concentration losses. The mass flow of hydrogen and air is regulated by two compressors which are controlled by two PI controllers to maintain a desirable pressure level within the FC. The dynamic behaviour of the FC model is determined by three effects. First, the current slope of the fuel cell is limited externally to avoid the fuel starvation phenomenon leading to high degradation of the FC membrane. The second effect is the cell internal voltage step response. While bipolar plates and the PEM can be represented by pure resistors, the catalyst material and gas diffusion layers (GDL) contain a capacitive effect providing an effective time constant for fuel cell step response. As the time constant is in the range of several milliseconds 16,19 , this effect only has a minor influence. The third effect influencing the fuel cell voltage response is a consequence of the implemented pressure and temperature control. Deviations in pressure or temperature are changing the OCV following the pressure and temperature dependent part of the Nernst equation. As a result, the dynamic part of the FC voltage mainly follows the pressure oscillations of the pressure control which is also observed in literature. To include the capacitive effect of the catalyst and the GDL, the resulting time constant has been approximated by a first order delay of the FC voltage response. More detailed informations about the FC model can be found in Dotzauer.

2.3 DC-DC converter

The bidirectional DC-DC converters are modelled on a system level, assuming an ideal inner current control and therefore neglecting any switching behavior and duty cycle control. As a result, the current at the input of the DC-DC converter can be set directly. The model equals the power on both input and output considering a user defined efficiency. Optional capacitors at the input and output of the converters were added to test if the capacitances of the converter have an impact on the stability of the control.

2.4 Cable

The cable model contains an electric resistor and an optional capacitance, which is sufficient for control tests. For efficiency and overall sizing studies, the influence of the cable length, current and voltage will be included.

2.5 Electric Machine

The model of the electric machine is part of the actuation library, which is a Modelica based library for electromechanical actuators (EMA) for aircraft and helicopters, developed by the DLR, the University of Nottingham and other partners in order to provide a set of standardized, modular, scalable and also validated EMA modules. 11 The electric drive used in the powertrain contains a permanent magnet synchronous motor (PMSM), an inverter and control. The used inverter model is an ideal non-switching inverter. As the switching and pulse width modulation process is removed, there are no losses between the DC and AC power and an ideal generation of AC currents is assumed. User defined losses or conduction losses due to switching can be included and are especially getting important in efficiency calculations. The PMSM model describes the behavior of the machine considering iron-losses and copper-losses and thermal behavior, but neglecting magnetic saturation and torque ripple.⁷ More detailed information about the inverter end electric motor can be found in Hill et al⁷. The cascade control of the electric drive consists of an outer speed control and an inner current control. The speed control allows a rotational speed setpoint input and the controller output is the desired rotating field oriented current setpoint Iq for the current controller. The current control is implemented as a field oriented control, including the transformation from 3 phase current to the field orientated I_d and I_q currents (park transformation) that are controlled by two PI controllers with anti-windup and the following inverse park transformation retransforming the I_a and I_d current output back to 3 phase current for the inverter. As a result, the electric drive model can provide dynamic results. The model is only used in the non field weakening operational field, which means

that the I_d current setpoint is always zero. Therefore, positive or negative I_d currents only appear in transients as a result of the control. The inverter model as well as the PMSM are fully bidirectional allowing motor- and generator operation.

3. Architectures and control tests

The following section shows multiple examples of different architectures and control tests as a possible use case of the powertrain model.

3.1 Voltage and current control

The most simple powertrain configuration includes one electric drive, one FC, and one auxiliary battery to compensate occurring power imbalances as a result of dynamic restrictions of the FC. A 3.5 h long mission is used containing takeoff, climb, cruise and descent and an additional go around with again climb cruise and descent, shown in figure 2. While the propeller torque is relative constant throughout the mission, the rotational speed is changing, implicating a lower propeller pitch angle at takeoff and a higher pitch angle at cruise.

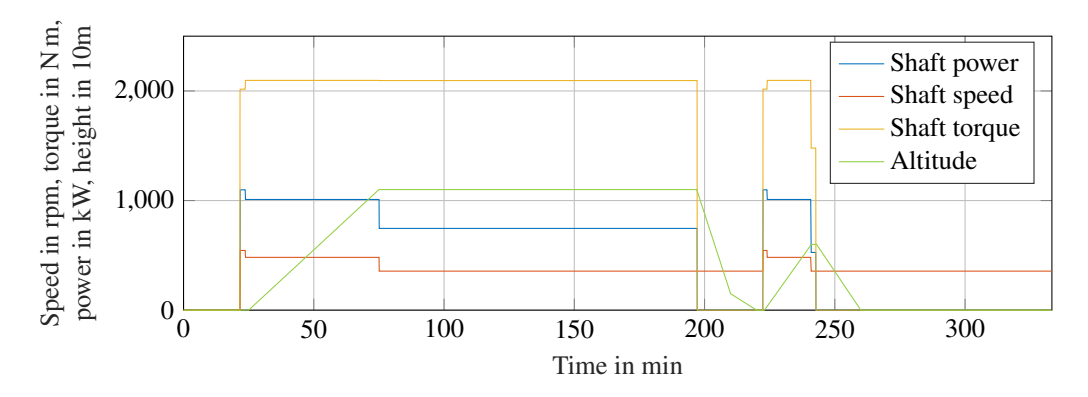


Figure 2: Mission power composed of motor shaft speed and torque.

Two control concepts have been tested, a simple voltage control, where both battery and FC are connected to the grid via DC-DC converters and a current control, where the battery is directly connected to the grid resulting in a floating grid voltage. In figure 3, the two control concepts are shown. DC-DC converters and a control forming the power distribution unit are controlling the power distribution between the battery and fuel cell.

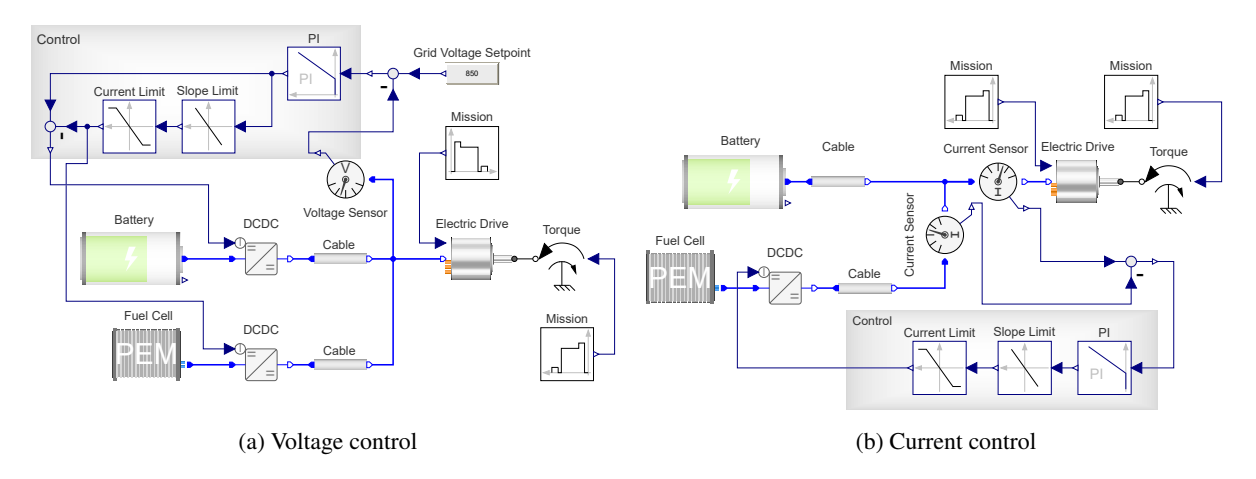


Figure 3: Block diagram of voltage control with two DC-DC converters in (a) and current control with one DC-DC converter and floating voltage in (b).

In case of the voltage control in figure 3(a), the controller output sets the battery and FC current. The set current output is divided between the different power sources in such a way, that the FC supplies 100 % of the set current, but is constrained by a certain current slope. Accordingly, the FC current set value is constrained by a slew rate limiter and

a minimum and maximum limit value. The resulting current difference between the current setpoint and the FC current is used as the setpoint for the battery DC-DC converter setting the battery current. In figure 3(b), the battery is directly connected to the grid. Here, the power distribution is controlled by a current control where the current set value of the FC DC-DC converter is the motor current but is again restricted by a certain current slope.

In figure 4, two different behaviours of the grid voltage over the duration of the mission in case of voltage control and current control can be observed. For the voltage control, in steady state the voltage is exactly at the setpoint voltage. In load transients, the current of the electric drive changes, leading to a decrease or increase in grid voltage to which the control can react. This leads to the voltage peaks in figure 4. The magnitude of these voltage peaks depends on the controller gain and on the load power slew rate. In case of current control, the measured motor current is the control setpoint and the FC current the measured value. The controller output is again constrained by a current slope and maximum and minimum current. Because of the direct connection of the battery to the main grid, any current difference between the FC current and motor current is automatically flowing through the battery without any further control. In this case, there are no voltage peaks occurring in the grid voltage during the mission. Instead, the grid voltage depends on the battery's SOC and due to its internal resistance on the current passing through it. Although the system may seem simpler in case of partial active topologies, active power management not only offers better control over the power distribution but also increase system safety⁹ e.g. by preventing deep discharge of the battery or by using DC-DC converters capable of limiting fault currents to minimize the need for load side circuit breakers.¹

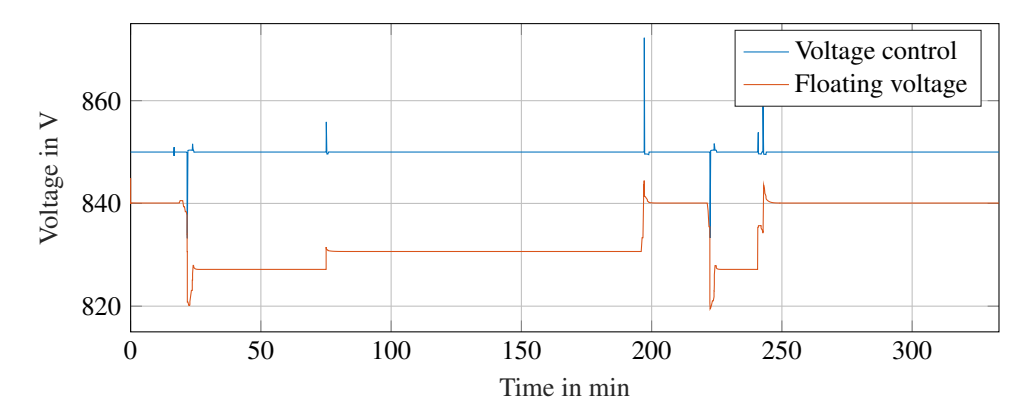


Figure 4: Grid voltage of voltage control and floating voltage current control.

In figure 5, the power of the battery, FC and electric motor throughout the mission is shown. As the FC current slope is limited, the FC can not instantaneously provide the power demand during a power step up to maximum power. Therefore, the battery has to provide the missing power and shows a triangular shaped power profile. The opposite behaviour occurs in case of a power step down, where the power surplus of the FC is used to charge the battery again.

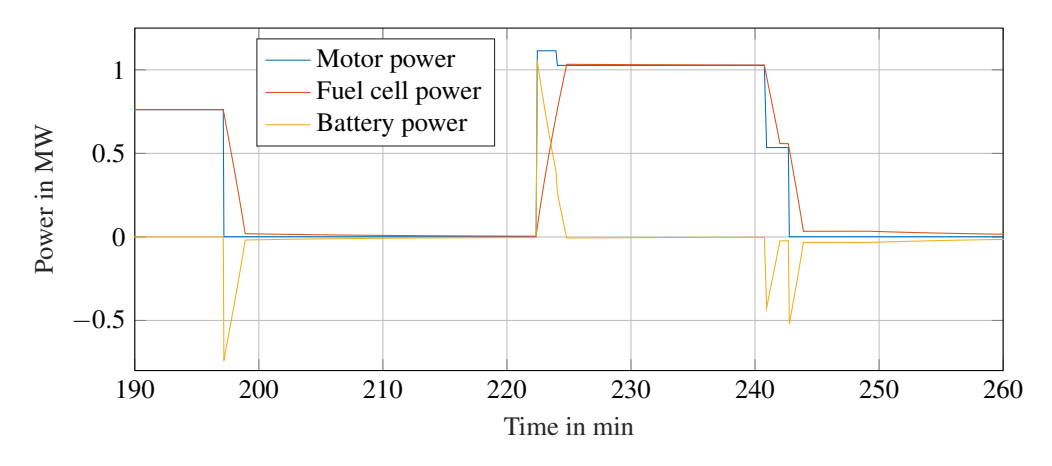


Figure 5: Power throughout the mission of the electric motor, the FC and the battery.

The powertrain can be extended to include multiple batteries, fuel cells and electric motors to simulate larger distributed propulsion grids using the same control concepts. In this case, battery charging strategies can be included by manipulating the battery setpoint currents depending on the state of charge of the batteries. In case of an optimal battery weight, it is best to keep the battery fully charged. Given a maximum allowed C-rate, the same battery can

deliver more power fully charged because of the higher OCV and has in this state its highest temporary power density. In case of a sudden shutdown of the electric drive, a power surplus exists because of the current slope restrictions of the FC. In this case, the battery needs to be able to absorb the power surplus of the FC, not exceeding its defined maximum SOC e. g. 0.9 C. This problem can be solved by calculating the battery charge current not only dependent on its SOC, but also on the current power demand of the electric motors. This leads to a SOC profile shown in figure 6, where the battery is always loaded to the maximum SOC, where the battery does not exceed its maximum SOC level in case of a sudden ramp down of the fuel cell. By comparing the motor power with the SOC, the correlation between the current motor power and the charging level can be observed. E. g. the charging limit at 100 min is higher that at 50 min because of the change in motor power from climb power to cruise power. By using this charging strategy, a SOC balance between the different battery stacks is automatically included. To show the balancing effect, the two batteries used in this simulation have two different initial SOC levels of 1.0 and 0.8, shown in figure 6.

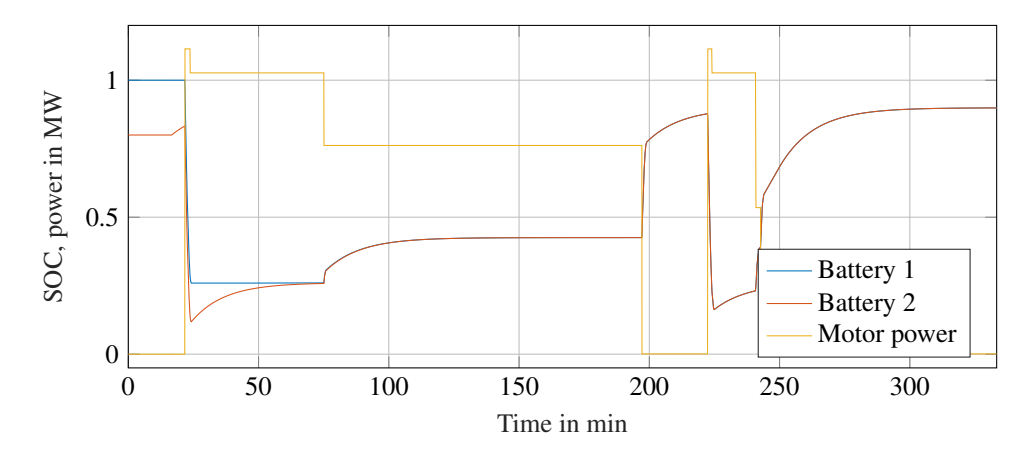


Figure 6: Battery SOC with different initial SOC and simple battery management system (BMS).

3.2 Battery balancing using droop control

Droop control can also be used to archive the desired power distribution strategy. In figure 7, the architecture and control is shown, including two batteries, one FC and one electric drive. The FC current is regulated by a current control similar to the architecture shown in figure 3(b). The currents of the two batteries are controlled using droop control and a virtual droop resistor. This concept has the advantage, that the individual controls are independent from each other and don't need to communicate.

In the mission power profile shown in figure 8, a similar interaction of the different components can be seen. According to figure 9(a), there is no floating voltage or permanent voltage droop unlike in other droop control use cases. Because the batteries provide zero current in stationary phases, the voltage is in this case at its maximum value which is the desired grid voltage. The voltage only differs from the set voltage in case of FC ramp up or ramp down when the battery is active, the amount is dependent on the droop characteristic of the voltage current curve.

Battery SOC balance can also be achieved using this control method by manipulating the virtual droop control resistances depending on the SOC of the battery and the sign of the battery current. Different from the voltage control approach, the droop control and implemented battery balancing is only active if the battery is used. In stationary phases, the balancing is not active. The different battery SOC over the mission with balancing is shown in figure 9(b).

4. Battery size estimation

The powertrain simulation can also be used as a verification tool for component sizing, e.g. for battery sizing, which is described in this section 4.2. Differences in operation strategies leading to different maximum battery power or energy can have a big influence on the battery weight. To get an overview about different battery masses and their dependencies, an analytical calculation was done as a preliminary stage to the simulation. The size of the battery is mainly defined by two factors. First, the battery must contain enough energy to not fall below the minimum SOC of the battery throughout the mission (energy constraint), and second, the battery also must not exceed the maximum allowed C-rate (power constraint). If the battery is used as a main power source, the battery mass m_{battery} is defined in most cases by the energy constraint using eq. (3):

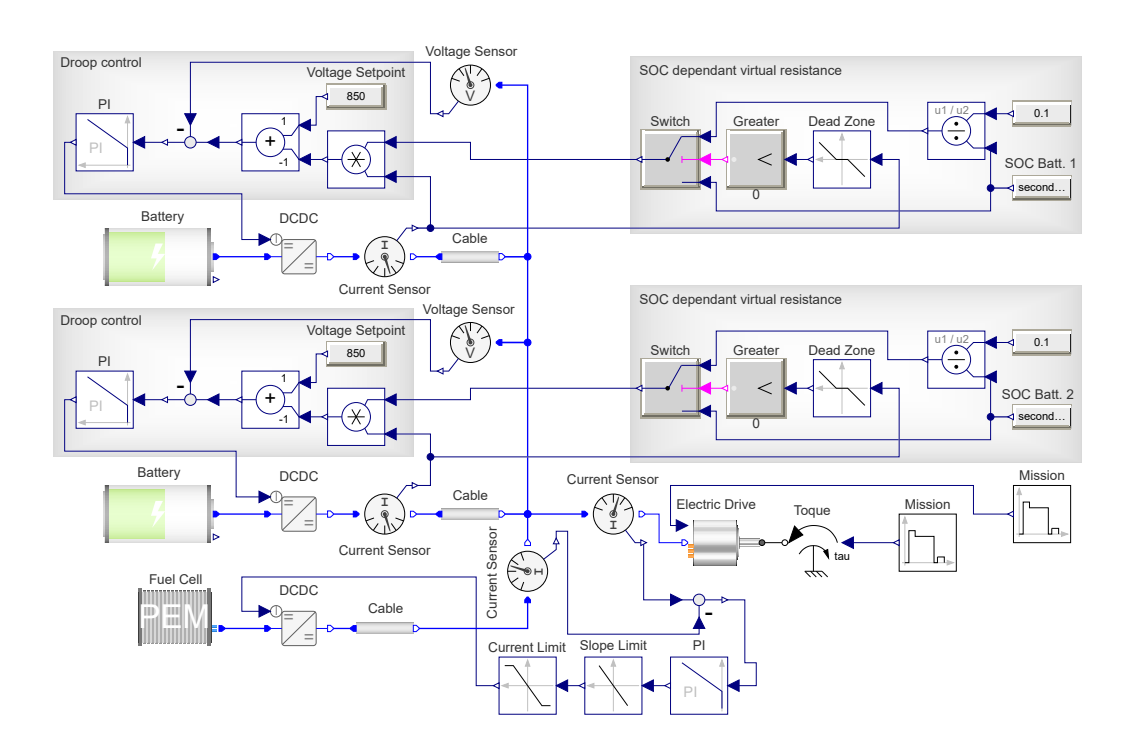


Figure 7: Block diagram of partial droop control architecture.

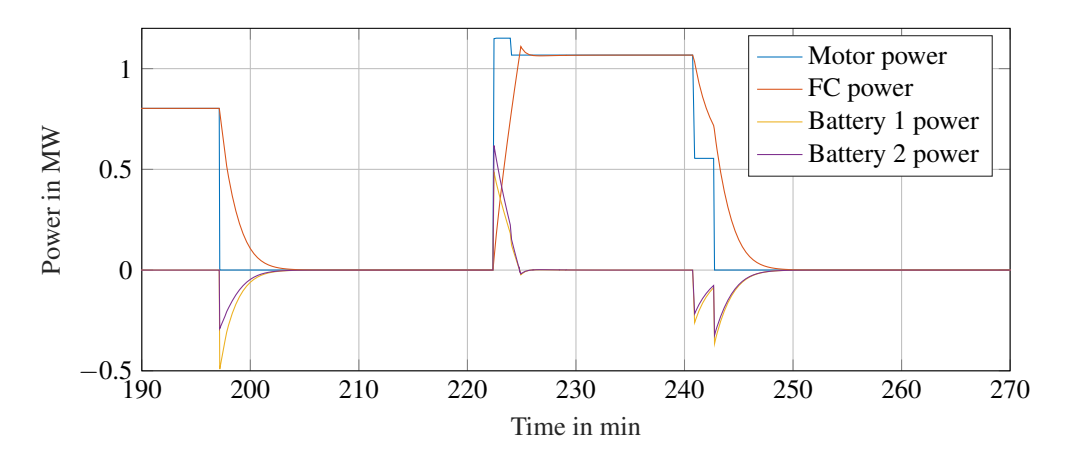


Figure 8: Power distribution using partial droop control.

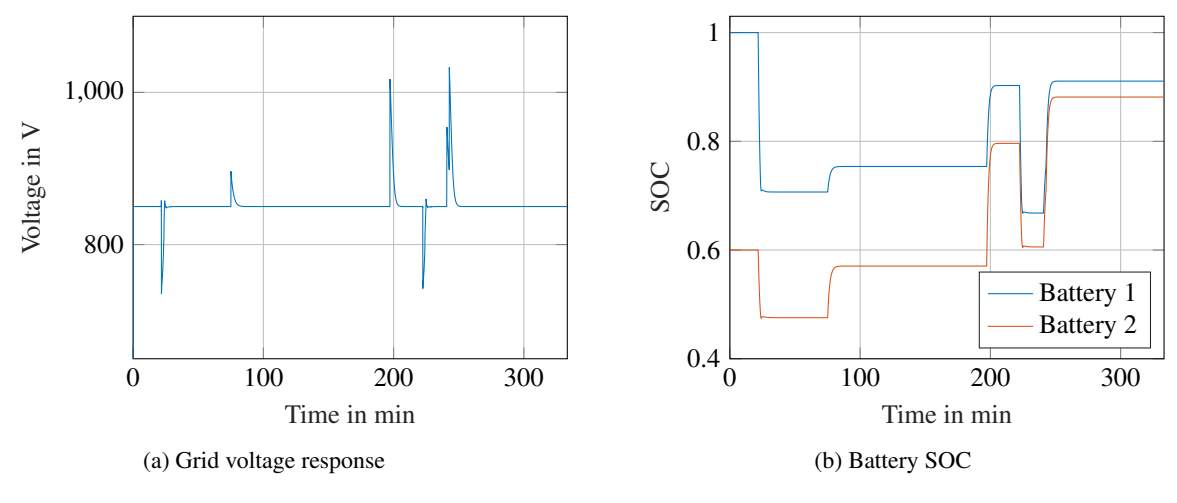


Figure 9: Grid voltage using partial droop control in (a) and corresponding battery SOC in (b).

$$m_{\text{battery}} = \int \frac{P(t)}{E_{\text{density}}} \, dt$$
 (3)

where $E_{density}$ is the gravimetric energy density of the battery and P(t) the power of the battery throughout the mission. If the battery is only an auxiliary power source and only supplies power in transients, as discussed in section 3, the power constraint of the battery gets important. The minimum battery mass based on the power constraint can be calculated using eq. (4):

$$m_{\text{battery}} = \frac{P_{\text{max}}}{E_{\text{density}}C_{\text{rate}}} \tag{4}$$

where the C-rate is the maximum allowed current divided by the capacity of the battery and P_{max} the maximum power the battery has to deliver. In general, the maximum of eq. (3) and eq. (4) is the minimum battery weight. While the energy constraint battery mass mainly scales with the energy density, the power constraint battery mass is also dependent on the maximum allowed C-rate. In the following considerations, an exemplary power step of 1 MW is used to calculate the necessary battery mass at variation of the FC ramp time, which is the time the FC needs to ramp up its power from 0 % to 100 %. This results in the typical triangular power profile of the battery shown in figure 10, with an exemplary FC ramp time of 60 s.

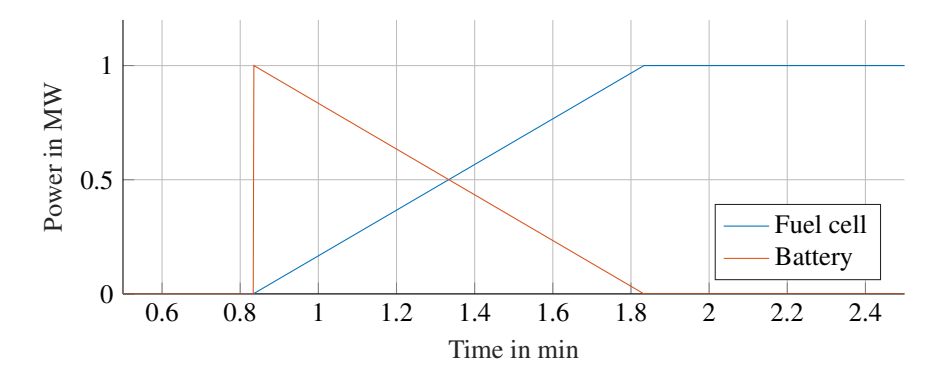


Figure 10: FC power ramp up and auxilliary battery power source.

There are many different lithium ion battery types like NCA, NMC, lithium iron phosphate (LFP), lithium cobalt oxide (LCO), Lithium Manganese Oxide (LMO) and LTO.¹⁴ The C-rates and energy density specifications of these batteries differ a lot, not only among the different battery types but also within one battery chemistry. As the maximum allowed discharge current primarily has an influence on the battery lifetime, there is no fixed C-rate limit for a battery, it always depends on the desired cycle number. This makes it difficult to compare battery specifications, especially when the number of cycles is either different or not specified. Although across all the different battery specifications, there is always a tradeoff between energy density and power density. However, the available battery specifications differ to much to provide e. g. a battery type specific typical power density value. For this reason, it makes more sense to show the different dependencies instead of calculating actual battery masses based on manufacturer specifications. To get actual values, the chart shown in Dechent et al³ has been used. Based on this battery comparison, regions of high energy density and high power density batteries can be observed and chosen as reference batteries. For the high energy density battery, an energy density of 230 Wh/kg and a C-rate of 1 C is chosen which can be for example a NCA or NMC type battery (which is used as a high energy density reference battery, called NMC battery from now on). For the high power density battery, a LTO battery with an specified energy density of 45 Wh/kg and a C-rate of 21 C is chosen (which is used as a high power density reference battery, called LTO battery from now on). As the voltage of a fully charged LTO battery is higher than its nominal cell voltage, the temporary energy density at a SOC of one is higher than 45 Wh/kg. Concerning a nominal Voltage of 2.3 V and an OCV of 2.8 V when fully charged, the temporary energy density of a fully charged LTO battery is 55 Wh/kg. For comparison, supercapacitors (SC) are also included in the calculations with a comparatively low energy density of 5 Wh/kg and a C-rate of 400 C.

Figure 11 shows the battery mass based on the power constraint over the C-rate, showing the strong influence of the C-rate on the battery mass because of its hyperbolic curve. Under consideration of the mentioned C-rate limits, the resulting battery mass is 4348 kg for the NMC battery, 1058 kg for the half charged LTO battery, 869 kg for the fully charged LTO battery and 250 kg for the SC. The mass difference between a half and fully charged LTO battery is 18%. As only the power constraint (eq. (4)) is considered in figure 11, the different battery masses are in this case independent from the FC ramp time leading to a horizontal curve in figure 12 (dotted lines at 869 kg and 250 kg). Figure 12 shows

the different electric storage masses, LTO battery, SC and LTO-SC-combination over the FC ramp time. As the NMC battery weight is outweighing the LTO battery by a factor 5 and the SC by a factor 17, it is not suitable for auxiliary power supply compared to LTO and SC and is therefore not shown in figure 12. In the following calculations, the energy density of a fully charged LTO battery of 55 Wh/kg is used. Eq. (3) leads to a linear dependency of the battery mass on the FC ramp time shown in figure 12 with a higher gradient for the SC and a lower gradient for the LTO battery. The maximum out of eq. (3) and eq. (4) is the minimum battery weight for a given FC ramp time using only LTO batteries or only SC batteries shown in figure 12 (LTO in blue, SC in green).

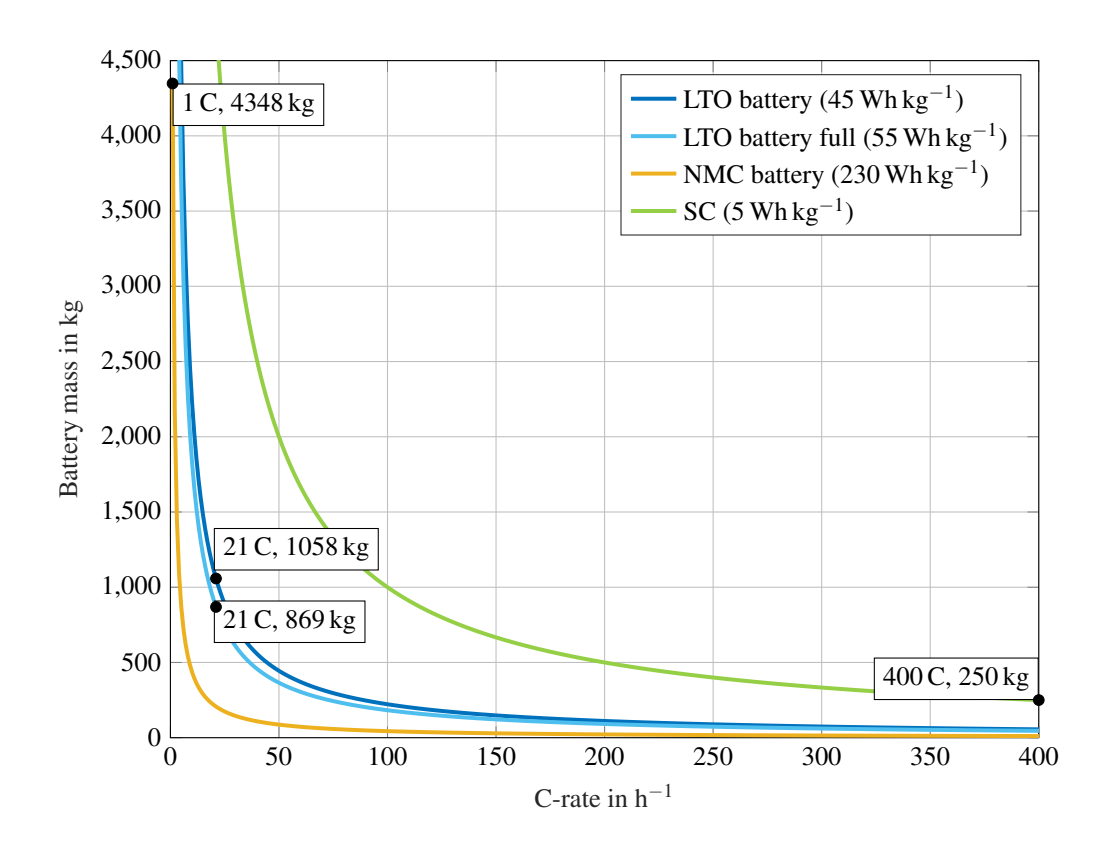


Figure 11: Battery mass based on maximum allowed C-rate.

4.1 Combination of SC and LTO battery

To optimise the system, a combination of SC and LTO battery might be beneficial. In this case, the SC part of the electric energy storage reduces peak currents in the battery in case of short power peaks, reducing the battery current and therefore its mass, but also having the additional mass of the SC. In the following calculations, the power is distributed between LTO and SC by a horizontal line in the power over time plot shown in figure 13, where blue area highlights the power provided by the battery and the red area highlights the power provided by the SC. The location of the horizontal distribution line is defined by a factor f, which can be 0 when the power is only supplied by the SC and 1 when the power is only supplied by the LTO battery. A factor of 0.5 means the power is equally distributed between the SC and the LTO battery at the time of the power step. To get the minimum combined electric energy storage mass for a given FC ramp time, the factor f is varied between 0 and 1 searching for the lowest combined mass while each are fulfilling the power and energy constraint. This minimum combined battery mass (figure 12, LTO and SC combination) and its composition of LTO mass (figure 12, LTO part) and SC mass (figure 12, SC part) is shown in figure 12.

As a result, for low FC ramp up times, in this calculation up to 9 s, it is best to only use SC, and for FC ramp up times over 343 s it is best to only use LTO batteries. In between, a combination is beneficial, but only showing a big potential between 20 s and 80 s. As an example, for a given FC ramp time of 50 s, the combined electric energy storage mass is 733 kg, consisting of 595 kg LTO battery and 138 kg SC. A distribution factor of 0.68 turned out to result in the lowest combined battery weight for the FC ramp time of 50 s. Compared to 869 kg if only LTO is used, a combination

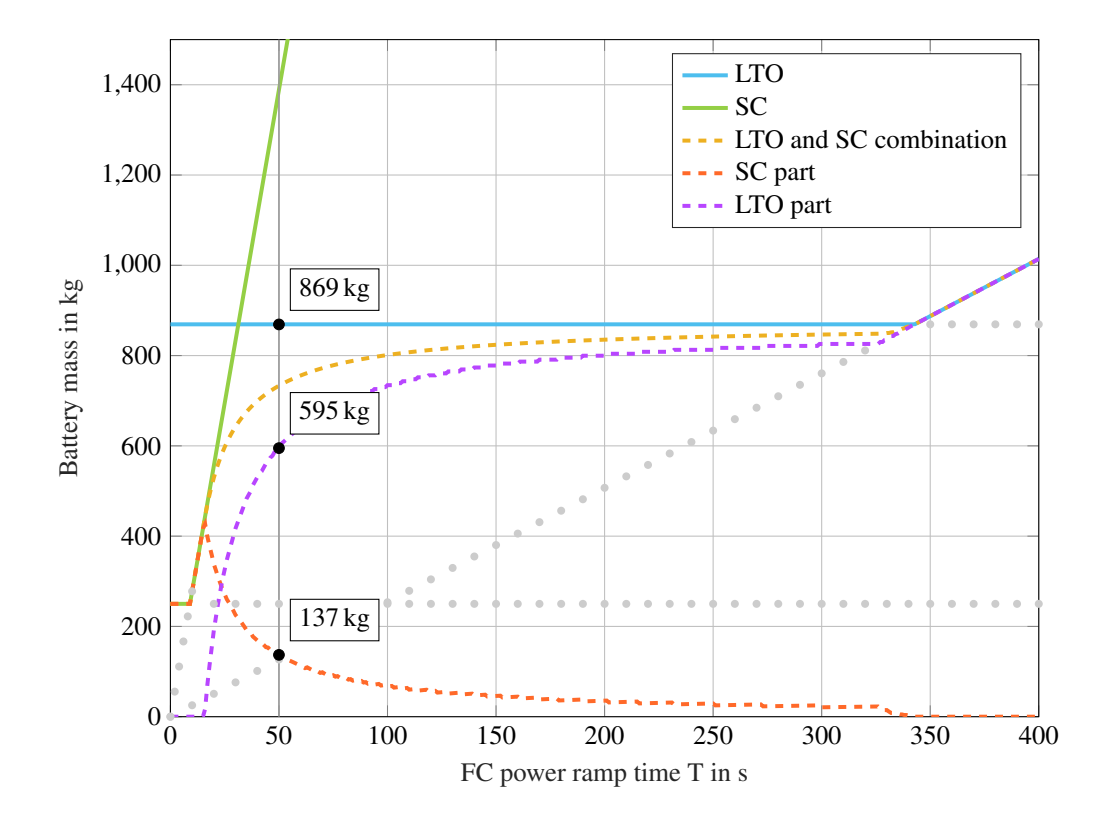


Figure 12: Battery masses considering both energy constraint and power constraint for LTO battery, SC and the combination of both.

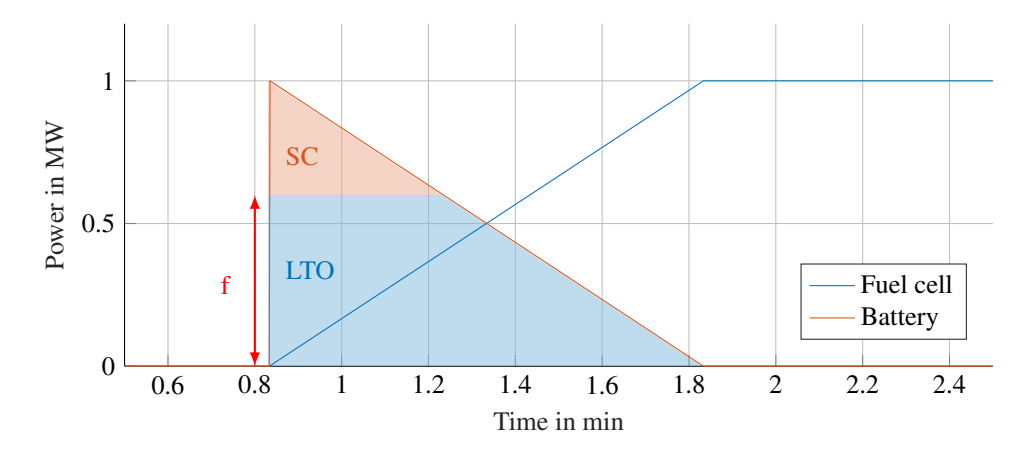


Figure 13: FC power ramp up and auxilliary battery power supply distributed between LTO and SC by a factor f.

can save about in this case about 16 % of battery mass.

Parameter variations show their influence on the battery mass diagram. The energy density of the battery alters the gradient of the energy constraint curve. Restricting the battery SOC range also alters the gradient of the energy constraint curve but has no significant influence on the power constraint curve. The horizontal power constraint curves are mainly affected by the energy density and the C-Rate. Changing the 1 MW power-step to a power-ramp with a few seconds rise-time only has a minor affect, as the maximum power peak barely decreases.

4.2 Battery mass verification using the powertrain model

The powertrain can also be used for component sizing and can be used to verify the results of section 4 and 4.1, also taking dynamic effects and other SOC dependent effects into account that might be overlooked or neglected in the analytical approach. Therefore, a simple power step of 1 MW is simulated, using only a LTO battery and a combination of LTO and SC. The get the desired power distribution factor of 0.68, a current limit for the LTO battery is implemented and adjusted. As the simulation does not contain any automatised parameter optimisation, the capacity of the LTO battery and SC is adjusted manually. To get the minimum battery weight, the individual capacities are lowered as far as possible without violating the C-rate limits. The minimum capacity and therefore the minimum battery weight is reached within a few simulations.

In figure 14 and figure 15, a FC ramp up time of 50 s is buffered by only using an LTO battery in figure 14 and by a combination of LTO and SC in figure 15.

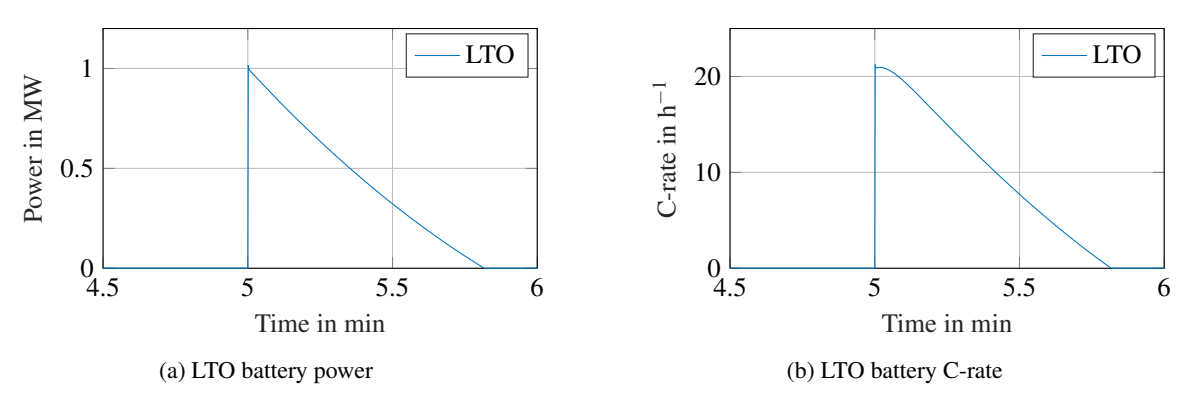


Figure 14: The power profile in (a) and C-rate in (b) of LTO battery during a power step.

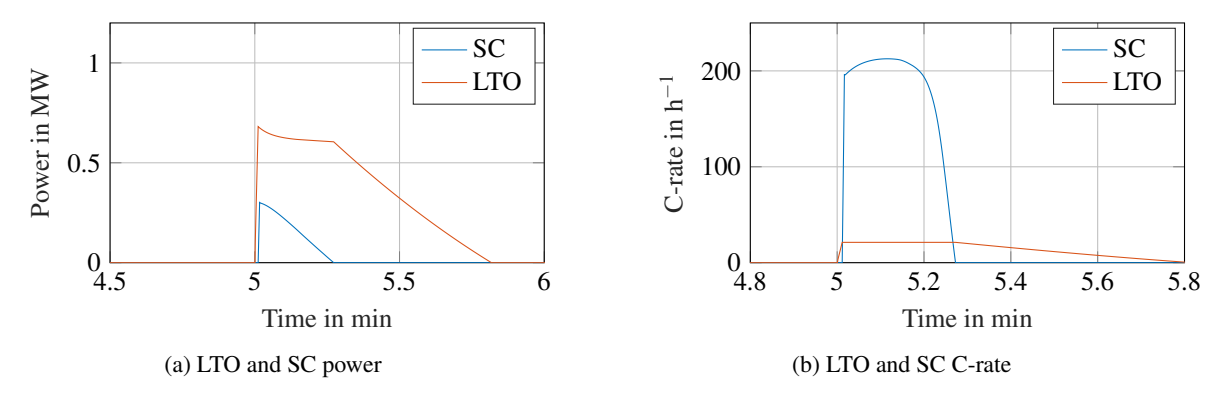


Figure 15: The power profile in (a) and C-rate in (b) of LTO battery and SC in combination during a power step.

In figure 14(a) the triangular shaped load power profile is shown. A small deviation from the triangular shaped power profile can be observed which results from the FC polarisation curve where the voltage decreases with an increasing current. Sizing the battery to have 21 C maximum at peak power (figure 14(b)) gives a result of 872 kg matching the analytical result of 869 kg fairly good. In figure 15, the previous calculated optimal distribution factor of 0.68 is used to split the power between the LTO and SC, shown in figure 15(a). As the SOC dependent voltage of both battery and SC is considered in the simulation, the results differ from the analytical results. For the LTO battery, the maximum current sets the C-rate of the LTO battery to 21 C for about 20 s shown in figure 15(b), while the power decreases because of the decreasing open circuit voltage during discharge. This in turn alters the SC power profile,

differing from the previously assumed triangular shaped power profile. As the voltage of the SC linearly decreases down to zero during a discharge cycle, the C-rate does not necessarily decrease after the highest output power and can even increase, as shown in figure 15(b). This is further intensified by the decreasing power output of the LTO battery during discharge, not considered in the analytical calculation. Also not considered in the analytical calculations is an internal resistance of the SC, lowering the output voltage and therefore the output power at a fixed C-Rate, which especially gets important at high C-rates and therefore high currents. All these effects are forcing the SC to be oversized and has a mass of 160 kg instead of the analytically calculated 138 kg. Considering a minimum state of charge of the SC defined by the minimum input voltage of the DC-DC converters, its mass will eventually further increase. The difference in weight of 15 % shows the importance of dynamic simulation of the powertrain.

5. Conclusion and outlook

In this paper, a dynamic model of a hybrid electric powertrain and its components developed in Modelica were explained, showing the possibility of simulating gate to gate missions and possible examples of use cases like control development and component sizing.

While doing a battery sizing estimation, especially with a combination of different battery types, a manual calculation gets rapidly more complex by including more dependencies, also increasing the risk of missing important constraints resulting in wrong results. The powertrain simulation makes it easy to check relevant constraints while inheriting many dependencies like variable open circuit voltages, internal resistances, realistic and not ideal power ramps and so on, which are not implemented in the analytical calculations. This makes the powertrain a flexible and fast sizing tool for various components. The results show, that the auxiliary battery mass is mainly affected by the maximum allowed C-rate of the battery. The use of SC and the combination of both is mainly beneficial in cases with low FC ramp times.

Furthermore, the powertrain can be used to implement and test different control concepts. Section 3 shows that the powertrain can be controlled by a simple voltage control as well as current control or partial droop control with included battery stack balancing.

To cover the complete powertrain of a hybrid electric aircraft, the powertrain simulation will be extended to include not only the electric components but also a gas turbine, a propeller, a gearbox and a cooling channel, especially important for use cases with fuel cells. This allows overall efficiency calculations and comparisons of different operation strategies including failure cases.

6. Acknowledgement

The project is supported by the Clean Aviation Joint Undertaking and its members in the framework of Grant Agreement no 101102020 - AMBER



Funded by the European Union. Views and opinions expressed are however those of the author(s) only and do not necessarily reflect those of the European Union or Clean Aviation Joint Undertaking. Neither the European Union nor the granting authority can be held responsible for them.



References

- [1] Pietro Cairoli, Rostan Rodrigues, and Huaxi Zheng. Fault current limiting power converters for protection of dc microgrids. In *SoutheastCon 2017*, pages 1–7. IEEE, March 2017.
- [2] Maria Cristina Cameretti, Andrea Del Pizzo, Luigi Pio Di Noia, Michele Ferrara, and Ciro Pascarella. Modeling and investigation of a turboprop hybrid electric propulsion system. *Aerospace*, 5(4):123, November 2018.
- [3] Philipp Dechent, Alexander Epp, Dominik Jöst, Yuliya Preger, Peter M. Attia, Weihan Li, and Dirk Uwe Sauer. Enpolite: Comparing lithium-ion cells across energy, power, lifetime, and temperature. *ACS Energy Letters*, 6(6):2351–2355, June 2021.
- [4] Niclas A. Dotzauer. Dynamic modeling of fuel cells for applications in aviation. In *EASN 2024*, EASN 2024, page 68. MDPI, March 2025.
- [5] Robert W. Erickson. Dc-dc power converters, June 2007.
- [6] Giuseppe Grazioso, Mario Di Stasio, Fabrizio Nicolosi, and Salvatore Trepiccione. A mathematical model for hybrid-electric propulsion system for regional propeller-driven aircraft. *Energy Conversion and Management*, 26:100957, April 2025.
- [7] Christopher Ian Hill, Chris Gerada, Paolo Giangrande, and Serhiy Bozhko. Development of a modelica library for electro-mechanical actuator system studies including fault scenarios and losses. In *SAE Technical Paper Series*, volume 1 of *ASTC*. SAE International, September 2014.
- [8] M. Jung, M. D. Ashford, and K. A. Williams. Analysis of a fuel cell system by a step response. *Fuel Cells*, 11(2):327–338, December 2010.
- [9] Bohwa Lee, Poomin Park, Chuntaek Kim, Sooseok Yang, and Seokmin Ahn. Power managements of a hybrid electric propulsion system for uavs. *Journal of Mechanical Science and Technology*, 26(8):2291–2299, aug 2012.
- [10] Shuangqi Li, Pengfei Zhao, Chenghong Gu, Siqi Bu, Xiaoze Pei, Xianwu Zeng, Jianwei Li, and Shuang Cheng. Hybrid power system topology and energy management scheme design for hydrogen-powered aircraft. *IEEE Transactions on Smart Grid*, 15(2):1201–1212, March 2024.
- [11] Franciscus van der Linden, Clemens Schlegel, Markus Christmann, Gergely Regula, Christopher Hill, Paolo Giangrande, Jean-Charles Maré, and Imanol Egaña. Implementation of a modelica library for simulation of electromechanical actuators for aircraft and helicopters. In *Proceedings of the 10th International Modelica Conference, March 10–12, 2014, Lund, Sweden*, volume 96 of *Modelica*, pages 757–766. Linköping University Electronic Press, March 2014.
- [12] Seyed Saeed Madani, Erik Schaltz, and Søren Knudsen Kær. An electrical equivalent circuit model of a lithium titanate oxide battery. *Batteries*, 5(1):31, March 2019.
- [13] Ryan O'Hayre, SukWon Cha, Whitney Colella, and Fritz B. Prinz. Fuel Cell Fundamentals. Wiley, April 2016.
- [14] Sarthak Patnaik. Overview of electrode advances in commercial li-ion batteries. *Ionics*, 30(6):3069–3090, May 2024.
- [15] Manuel A. Rendón, Carlos D. Sánchez R., Josselyn Gallo M., and Alexandre H. Anzai. Aircraft hybrid-electric propulsion: Development trends, challenges and opportunities. *Journal of Control, Automation and Electrical Systems*, 32(5):1244–1268, June 2021.
- [16] Phillip J. Smith, William R. Bennett, Ian J. Jakupca, and Ryan P. Gilligan. Proton exchange membrane fuel cell transient load response. Technical report, Glenn Research Center, Cleveland, Ohio, 2021.
- [17] P. Thounthong, V. Chunkag, P. Sethakul, B. Davat, and M. Hinaje. Comparative study of fuel-cell vehicle hybridization with battery or supercapacitor storage device. *IEEE Transactions on Vehicular Technology*, 58(8):3892–3904, October 2009.
- [18] P. Thounthong and P. Sethakul. Analysis of a fuel starvation phenomenon of a pem fuel cell. In 2007 Power Conversion Conference Nagoya, pages 731–738. IEEE, April 2007.

POWERTRAIN SIMULATION

- [19] Phatiphat Thounthong, Stephane Rael, and Bernard Davat. Control strategy of fuel cell and supercapacitors association for a distributed generation system. *IEEE Transactions on Industrial Electronics*, 54(6):3225–3233, December 2007.
- [20] Manh-Kien Tran, Andre DaCosta, Anosh Mevawalla, Satyam Panchal, and Michael Fowler. Comparative study of equivalent circuit models performance in four common lithium-ion batteries: Lfp, nmc, lmo, nca. *Batteries*, 7(3):51, July 2021.
- [21] Yue Xia. Comparison and analysis of soc estimation based on first-order and second-order thevenin battery models based on ekf. *Academic Journal of Science and Technology*, 6(3):10–18, July 2023.